ENGINEERING SCIENCES

The International Journal of Engineering Sciences
Vol. 2, No. 2, 2026, pp. 234-250
ISSN 3104-8897

https://international-journal-of-engineering-sciences.jo

Drawn Lightwell Changes in an Aqaba Commercial Building and Geometric Tests of Rectangular Apertures

Wesam Ali Bataineh,[1] Fawzy Ibrahim Bani Melhem,[2] Jebreel Esqoor[3]

[1] Department of Civil engineering, Yarmouk university, eng.wesam_bataineh4@gmail.com

[2] Department of Civil engineering, Yarmouk university, fazwzyfawzy.me@gmail.com

[3] Department of Civil engineering, Yarmouk university, jebreel.esqoor.eng@gmail.com

*** Corresponding Author**: Wesam Ali Yousef Bataineh; eng.wesam_bataineh4@gmail.com

DOI: https://doi.org/

ARTICLE INFO

Article history
Received May 25, 2026
Revised June 18, 2026
Accepted Oct 10, 2026

Keywords
Lightwell geometry,
building renovation,
solid angle,
direct sky access,
drawing digitization,
commercial building,
Aqaba.

ABSTRACT

This study examines the lightwell reconfiguration of an existing commercial building in Aqaba, Jordan. The renovation was designed and carried out in early 2026, when the study was prepared. A calibrated audit of three architectural plan panels compared existing and proposed void areas across four floors and tested the sensitivity of the estimates to digitized boundary placement and alternative readings of an overlapping rear edge. Under the principal interpretation, the proposed void area was smaller by 40.5% on the first floor, 27.8% on each of the second and third floors, and 45.3% on the fourth floor. All alternative boundary interpretations yielded reductions at their nominal coordinates. For the shared second- and third-floor panel, the combined sensitivity bounds included a possible increase in void area when the conservative rear-boundary interpretation was paired with endpoint variation.

Using the scheduled dimensions, a 10.45 × 1.20 m strip accounted for 72.7% of the total area of the three proposed openings on each comparable upper-floor plan. An idealized aperture experiment compared the strip with a square of equal area. At depths of 3.10 and 12.26 m, the strip exposed 10.45% and 1.22% of the upper hemisphere to a centred observer, respectively, while the square exposed 15.82% and 1.30%. For the strip, the ranking of sensitivity along the two axes reversed when displacements proportional to the aperture dimensions were replaced by equal displacements in metres. The audit quantified changes in plan void area, and the experiment estimated geometric sky access for specified aperture shapes and viewing positions. A building-specific before-and-after assessment would require verified three-dimensional sky paths from matching observation points in both configurations.

This is an open-access article under the CC–BY-SA license.

ENGINEERING SCIENCES
The International Journal of Engineering Sciences
https://international-journal-of-engineering-sciences.jo
Vol. 2, No. 2, 2026, pp. 234-250
ISSN 3104-8897

1. Introduction

Reconfiguring internal voids during renovation changes the distribution of floor area and can alter the paths through which daylight reaches the building core [1]. In buildings bordered by adjoining construction on several sides, these paths are particularly important for spaces set back from the street frontage. Area schedules can document where openings are reduced, extended or relocated. The portion of sky visible through those openings depends on their geometry and the position of the observer [2, 3].

Atrium studies have identified cross-sectional geometry, height, roof transmittance, surface reflectance and glazing configuration as factors affecting indoor daylight [4, 5]. Acosta et al. (2014) distinguished direct sky contributions from reflected light in a predictive method for courtyards [6]. Ahadi et al. (2017) examined how lightwell shape, depth and orientation affect dynamic daylight metrics [7], while Bugeat et al. (2020) investigated reflective linings and light-redirecting devices [8]. Adel Nasab and Teimourtash (2023) considered geometric and optical design variables together in a residential optimization study [9]. These studies provide methods for assessing daylight performance when the required geometric and optical inputs are available.

This study was prepared in early 2026 alongside the design and execution of a lightwell renovation in an existing commercial building in Aqaba, Jordan. During this work, the project drawings provided the basis for a calibrated comparison of existing and proposed void areas, and the analysis software was used to model geometric sky access through rectangular apertures of specified dimensions.

The study addresses two questions. First, how much did the plan void area change between the documented configurations, and how sensitive is that estimate to alternative readings of overlapping boundaries? Second, how do aperture aspect ratio, vertical viewing distance and observer position affect the proportion of the upper hemisphere visible through a rectangular opening? The study documents the reconstruction and measurement of the void boundaries and uses a controlled aperture experiment to examine the effect of each geometric variable on sky visibility.

2. Case and source material

The study documents the redesign and implementation of the lightwell configuration in an existing commercial building in Aqaba, Jordan. The study was prepared in early 2026, during the same period in which the renovation was designed and carried out. The 19-page architectural drawing set includes area diagrams, floor plans, sections, elevations and details. The notes on sheet A-3 indicate that the building was constructed and licensed in 1983 and that its licence was renewed in 2023. The renovation design called for closing part of the existing lightwell system and introducing new openings. The study uses the terms “old” and “proposed” as defined in the drawing legend.

Sheet A-3 (PDF page 4) provided the primary basis for measuring void areas. It contains separate plan panels for the ground, first and fourth floors and a shared panel for the second and third floors. Floor plans and sections on PDF pages 5–9 and 11–13 provided level references. The elevations on pages 14–17 show one detailed street-facing elevation and

identify the other three sides as adjoining. The reproduced drawing excerpts omit title blocks, project and parcel identifiers, and contact details.

Sections A–A, B–B and C–C were used to verify level datums and establish reference distances for the geometric model. The available sections do not show paired old and proposed sky paths from the same observation points, including all intervening constrictions. This limits their use in the model to establishing reference distances.

The architectural drawing set was the sole source of project data. The title block on sheet A-3 lists 2025 as the drawing year, which is retained in the source citation (Architectural design office, 2025). A separate review stamp on the shared second- and third-floor panel bears the date "7/1/2026," reproduced as printed.

The study compared old and proposed void areas on the first through fourth floors. The ground-floor panel shows proposed opening A, but supplies no corresponding old boundary for a paired comparison. The second and third floors are reported separately, using the same geometric reconstruction from their shared plan. The paired comparison therefore covers four levels in one building and is based on three distinct plan readings. All comparisons are descriptive and deterministic.

3. Methods

3.1 Plan reconstruction and dimensional audit

The study used a raster image of sheet A-3 measuring 2,600 pixels along its long edge. Each plan panel was calibrated separately along the horizontal and vertical axes using the 15 m and 20 m dimensions of the rectangular reference footprint. Vertical calibration used the centres of the two ticks on the 20.00 m dimension line. In all three panels, the upper and lower ticks were located at $y = 79$ and $y = 698$, respectively. The horizontal line near $y = 681$ crossed the dimension line above the lower tick. Figure 1b shows the calibration points in an enlarged excerpt, and Appendix A records their coordinates alongside the manually digitized coordinates of the old openings.

The drawing legend and opening labels guided the identification of dashed and dash-dot outlines. Where old and proposed outlines partially overlapped, the legible boundary segments were used to reconstruct the old opening as a rectangle. The rear edge in the shared second- and third-floor panel and in the fourth-floor panel was the least clearly defined boundary. All opening footprints were represented as rectangles in the area calculations.

For each digitized opening, area was calculated as$A = (r - l)(b - t)s_x s_y$ where l, r,t and b denote the left, right, top and bottom coordinates, s_x and s_y are the horizontal and vertical scales in metres per pixel. Old opening areas were summed separately for each floor. Proposed opening areas were calculated independently from the dimensions shown on the drawings. The percentage reduction was calculated as $100\left(1 - A_{\text{proposed}}/A_{\text{old}}\right)$ Openings that recur on different floors were retained in each floor's calculation because each plan represents a separate cut through the building.

The study examined two sources of uncertainty, separately and in combination. The first concerned the placement of digitized endpoints. Each endpoint was varied by ± 4 pixels, equivalent to approximately ± 0.13 m. Eight transects across clearly visible vertical segments each identified one pixel with a grey level below 200. The endpoint variation was set wider than the observed stroke to account for uncertainty in aligning segments and

ENGINEERING SCIENCES
The International Journal of Engineering Sciences
https://international-journal-of-engineering-sciences.jo
Vol. 2, No. 2, 2026, pp. 234-250
ISSN 3104-8897

reading interrupted marks. Appendix A provides the transect coordinates and the rule for reproducing this deterministic sensitivity test.

The second source of uncertainty concerned the upper boundary of the old rear opening in the shared second- and third-floor panel and the fourth-floor panel. The nominal reconstruction extended the legible sides to $y = 84$, near the adjacent upper line. A full-depth scenario extended the sides to the footprint line at $y = 79$. A conservative partial-footprint scenario used $y = 122$, the near edge of the proposed strip, and counted only the portion below that edge. This cut excluded the overlapping band in which the old boundary could not be traced unambiguously. It served as a geometric cut-off for assigning area to the old opening. The endpoint bounds were applied to each scenario. The combined deterministic envelope spans the minimum and maximum reductions obtained across the tested boundary readings, endpoint variations and proposed dimensions. Its limits apply to the scenarios evaluated.

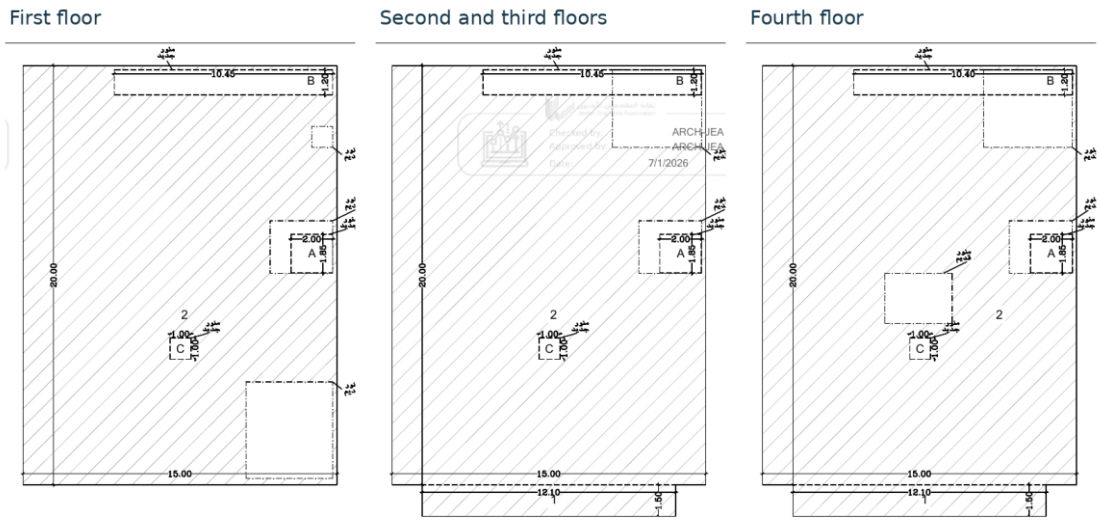


Figure 1a. Privacy-cropped extracts of sheet A-3, PDF page 4. The horizontal 15.00 m and vertical 20.00 m dimensions calibrate each rectangular panel. The three displayed panels document four levels. Figure 1b locates the two vertical calibration ticks. The source line key and a magnified audit of overlapping linework appear in Figure 2.

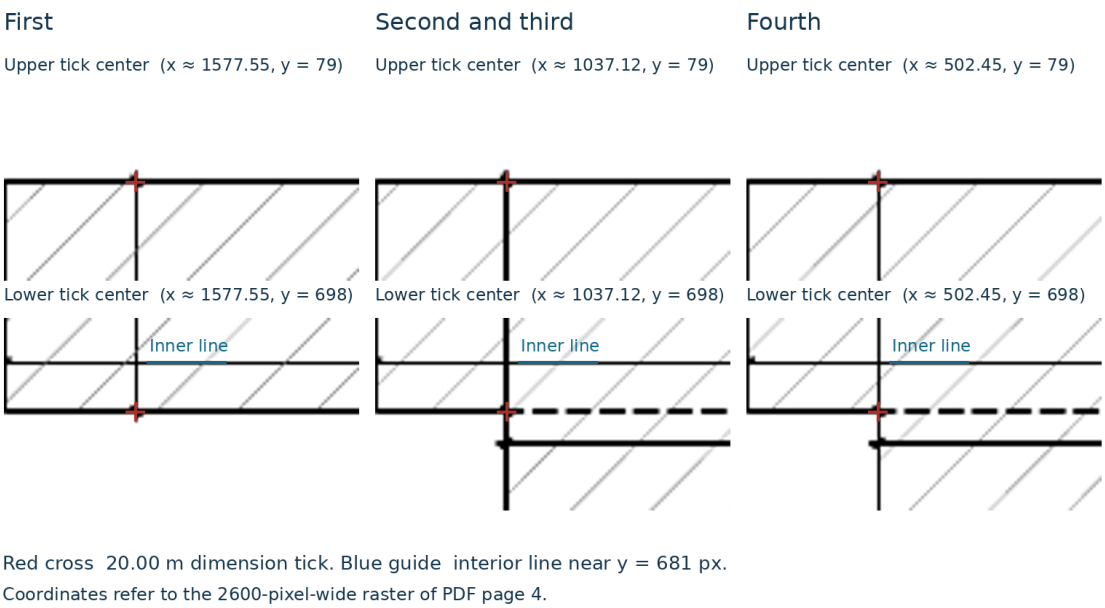


Figure 1b. Enlarged source excerpts showing the upper and lower ticks of the 20.00 m dimension on all three panels. The red crosses mark the tick centres. The blue guide marks the separate inner horizontal line near y = 681 pixels.

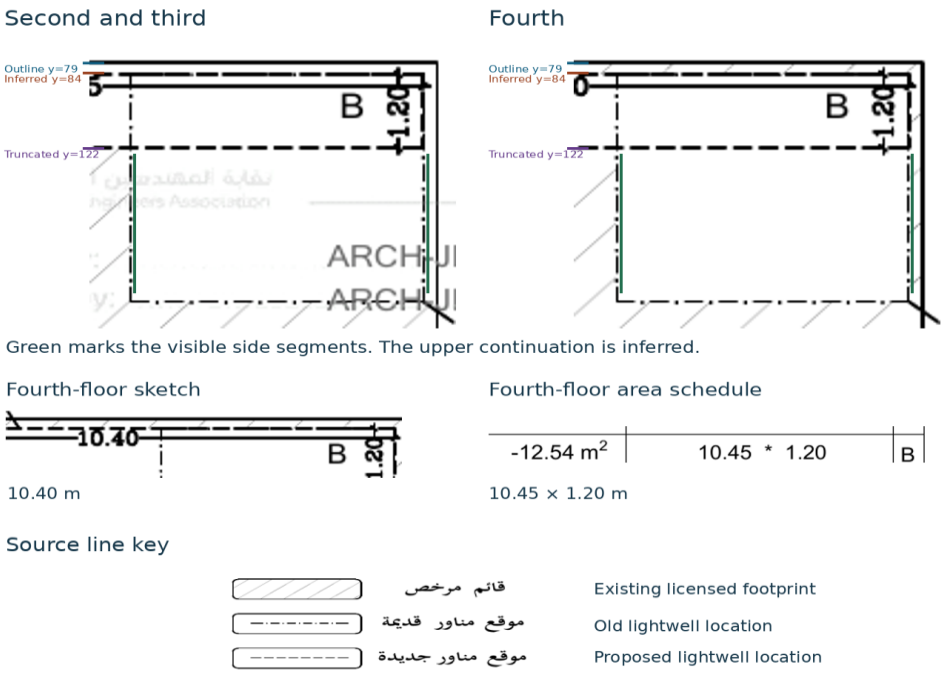


Figure 2. Source audit of the rear old rectangle and the fourth-floor length discrepancy. The green guides sit adjacent to visible old side segments below the overlap. Blue, orange and purple ticks locate the footprint edge, inferred rear boundary and conservative cutoff respectively in original raster coordinates. The lower extracts show 10.40 m in the sketch, 10.45 × 1.20 m in the schedule and the original line key with English translations.

ENGINEERING SCIENCES
The International Journal of Engineering Sciences
https://international-journal-of-engineering-sciences.jo
Vol. 2, No. 2, 2026, pp. 234-250
ISSN 3104-8897

The dimensional audit also compared the proposed opening dimensions annotated on the plans with those listed in the floor-area schedule. For opening B on the fourth floor, the plan gives a dimension of 10.40 m, while the schedule lists 10.45 m. Both values were carried through the upper-floor void-area comparison and the geometric sensitivity tests. The principal equal-area experiment used the scheduled value of 10.45 m.

3.2 Geometric aperture model

The study modelled each proposed rectangular opening separately as a horizontal aperture at the top of an idealized, unobstructed vertical prism. In the baseline comparison, the observation point was located directly below the centre of the aperture, on its vertical axis.
Reference depths were derived from the main roof datum of +15.89 m and the finished-floor datums shown in sections A–A, B–B and C–C on PDF pages 11, 12 and 13, respectively. Each section shows all five datums. Subtracting the first-, second-, third- and fourth-floor levels of +3.63, +6.59, +9.69 and +12.79 m from the roof datum yielded reference depths of 12.26, 9.30, 6.20 and 3.10 m, respectively.
The sensitivity analysis evaluated each aperture at all four reference depths. The resulting sky-access values describe the idealized aperture–depth combinations. The floor levels serve as dimensional references, and the constant cross-section is a modelling assumption specific to the idealized prisms.

The solid angle Ω of a rectangular opening of full length a and width b, viewed axially from depth h, is

$$\Omega = 4\arctan\left[\frac{ab}{4h\sqrt{h^2+(a/2)^2+(b/2)^2}}\right].$$

The study expressed the visible sky fraction as $\frac{100\Omega}{(2\pi)}$ where \Ω is the solid angle subtended by the aperture and 2π steradians is the solid angle of the upper hemisphere. For an off-axis observation point, Ω was calculated by integrating

$$\frac{h}{(h^2+x^2+y^2)^{3/2}}$$

over the aperture. Here, h is the vertical distance from the observation point to the aperture plane, and x and y are measured from the projection of that point onto the plane. The integrand follows from projecting each differential aperture element onto a plane perpendicular to its line of sight and dividing the projected area by the squared viewing distance. Appendix B gives the corner-based expression used to verify the off-axis calculations.

The **cosine-weighted sky fraction** weights each visible direction by the cosine of its zenith angle at a horizontal receptor. Its percentage is

$$\frac{100}{\pi}\iint_R \frac{h^2}{(h^2+x^2+y^2)^2}\,dx\,dy.$$

Under a sky of uniform luminance, the cosine-weighted fraction represents the ratio of direct sky illuminance on a horizontal receptor beneath the aperture to that on an unobstructed horizontal receptor under the same sky. The study compared the rankings obtained with the cosine-weighted fraction and the unweighted visible sky fraction to determine whether accounting for the angle of incidence changed the order of the aperture configurations.

The model assumes an unobstructed sky above the aperture and excludes solar position, temporal variation in sky luminance, surface interreflection and glazing transmission. Dynamic daylight metrics require time-resolved inputs (Reinhart et al., 2006). The lighting-energy calculation described by ISO and CIE (2024) also requires information on building use and lighting systems.

3.3 Controls and numerical verification

The study compared opening B with a hypothetical square of equal area to isolate the effect of aperture shape. The strip used in the principal comparison measured 10.45×1.20 m and had an area of $12.54\ \text{m}^2$ .The corresponding square had a side length of $\sqrt{12.54}$ m (approximately 3.54 m). For the sensitivity case using the plan dimension of 10.40 m, the square side was recalculated as as $\sqrt{12.48}$ m (approximately 3.53 m) to preserve equal area. The square served as a geometric benchmark. Its fit within the floor plan and its relationship to the rooms served by opening B were outside the scope of the comparison.

The study tested two off-axis displacement protocols for the nominal strip and its equal-area square. In the relative-displacement protocol, the observation point was shifted from the centred position by 40% of the aperture dimension along the axis being tested. For the strip, the offsets were 4.18 m along the long axis and 0.48 m along the short axis. For the square, the offset was approximately 1.42 m along either axis. In the fixed-displacement protocol, a 0.48 m offset was applied along each axis of both shapes. Each run varied the observation position along one axis at a time. A separate sensitivity test increased the model depth by 0.60 m while retaining the baseline aperture geometries. This test isolated the effect of increased vertical viewing distance within the idealized model.

The study verified the analytical solid-angle calculations against tensor-product Gauss–Legendre quadrature with 48 nodes per axis for all 16 centred aperture–depth combinations. The maximum absolute difference in visible sky fraction was below 10^{-10} percentage points. The cosine-weighted fractions changed by less than 10^{-8} percentage points when the quadrature resolution increased from 24 to 48 nodes per axis. A far-field check also recovered the leading-order approximation $\Omega \approx ab/h^2$, where a and b are the aperture side lengths and h is the vertical viewing distance. Verification was limited to numerical and analytical checks, with no field measurements.

4 . Results

4.1 Drawn void-area changes and sensitivity to boundary interpretation

Under the principal interpretation of the opening boundaries, void area decreased on every floor included in the paired comparison. These reductions remained positive throughout the ±4-pixel measurement bounds. Table 1 reports those bounds alongside the combined deterministic envelope for each floor. The fourth floor showed the largest nominal

The International Journal of Engineering Sciences
https://international-journal-of-engineering-sciences.jo
Vol. 2, No. 2, 2026, pp. 234-250
ISSN 3104-8897

reduction, although the overlap between the combined envelopes limits how confidently the floors can be ranked by percentage reduction.

Table 1. Plan void area under the principal reading and deterministic reduction bounds

Documented level	Old area (m^2)	Proposed principal (m^2)	Proposed alternative (m^2)	Principal reduction (%)	Measurement bounds (%)	Combined bounds (%)
First	28.95	17.24	—	40.5	28.5 to 50.0	28.5 to 50.0
Second	23.88	17.24	—	27.8	13.2 to 39.3	−14.2 to 40.9
Third	23.88	17.24	—	27.8	13.2 to 39.3	−14.2 to 40.9
Fourth	31.50	17.24	17.18	45.3	33.5 to 54.4	18.7 to 55.4

Measurement bounds hold the principal reading and schedule dimensions fixed. Combined lower bounds use the smallest old area and largest proposed area (17.24 m^2). Combined upper bounds use the largest old area and the smallest proposed area, 17.18 m^2 on the fourth floor and 17.24 m^2 elsewhere. Negative values denote an increase in proposed area. The second and third floors share one panel and one reading.

Table 2. Alternative rear-boundary readings and measurement stress tests

Panel	Reading (y in px)	Old nominal (m^2)	Old area bounds (m^2)	Nominal reduction (%)
Second and third	Outline (79)	24.56	20.50 to 29.15	29.8
Second and third	Principal (84)	23.88	19.87 to 28.39	27.8
Second and third	Truncated (122)	18.64	15.09 to 22.67	7.5
Fourth	Outline (79)	32.18	26.55 to 38.55	46.4
Fourth	Principal (84)	31.50	25.93 to 37.80	45.3
Fourth	Truncated (122)	26.31	21.20 to 32.13	34.5

Nominal reductions use 17.24 m^2 on both panels. For the second and third floors, even the nominal truncated reading exceeds 17.24 m^2. Its contracted lower area falls to 15.09 m^2, allowing a sign reversal under the joint stress test. The first and fourth floors retain reductions across all considered combinations.

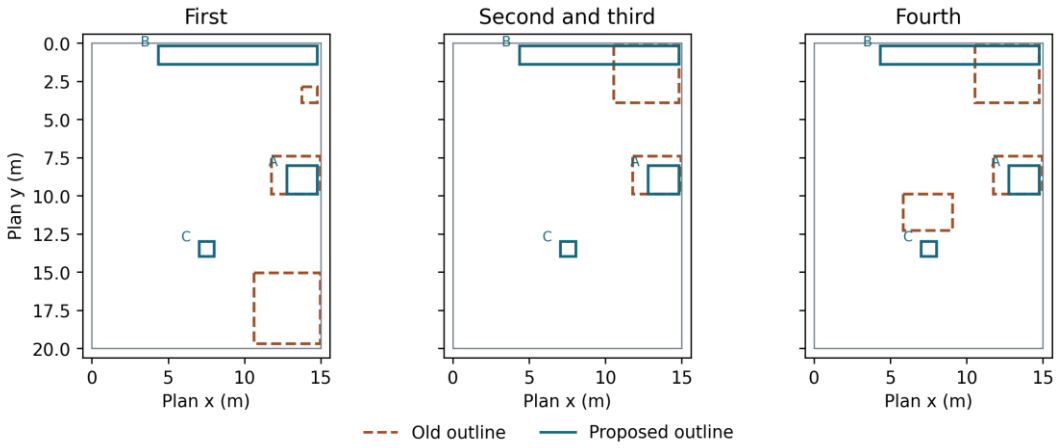


Figure 3. Analytical redrawings of comparable panels. The old outlines use the principal rear-boundary interpretation. A, B and C identify the proposed openings. The axes show local coordinates relative to each calibration rectangle.

The three proposed openings have distinct forms. A is near-square at 2.00 × 1.85 m (3.70 m²), B is a long strip at 10.45 × 1.20 m (12.54 m²), and C is square at 1.00 × 1.00 m (1.00 m²). B represents 72.7% of the sum of the three openings in each like-dimensioned upper-floor plan using the schedule values, and its length-to-width ratio is 8.71. Figure 3 shows that the proposed geometry partly overlaps old voids at A, extends a long opening along the back of the rectangular footprint at B and introduces C in a different part of the interior footprint. Area totals alone conceal that relocation and the concentration of most void area in B.

4.2 Aperture shape and observation depth

At every reference depth, B exposed more of the sky on axis than the physically smaller proposed openings A and C. Its aperture area makes a substantial contribution to that ranking. For B and the equal-area square, the controlled comparison reversed the ranking. At 3.10 m the strip exposed 10.45% of the hemisphere and the square 15.82%, a difference of 5.37 percentage points or a 34% reduction relative to the square. At 12.26 m the fractions were 1.22% and 1.30%, a difference of 0.08 percentage points or approximately 6%. The cosine-weighted fractions showed the same ordering. At 3.10 m they were 17.82% and 29.07%, respectively, a relative difference of 39%.

Table 3. Axial visible and cosine-weighted sky fractions at model depths

Model depth (m)	A visible (%)	B visible (%)	C visible (%)	Square visible (%)	B cosine-weighted (%)	Square cosine-weighted (%)
3.10	5.60	10.45	1.61	15.82	17.82	29.07
6.20	1.50	3.95	0.41	4.81	7.31	9.37
9.30	0.67	2.01	0.18	2.23	3.85	4.40
12.26	0.39	1.22	0.11	1.30	2.38	2.58

ENGINEERING SCIENCES
The International Journal of Engineering Sciences
https://international-journal-of-engineering-sciences.jo
Vol. 2, No. 2, 2026, pp. 234-250
ISSN 3104-8897

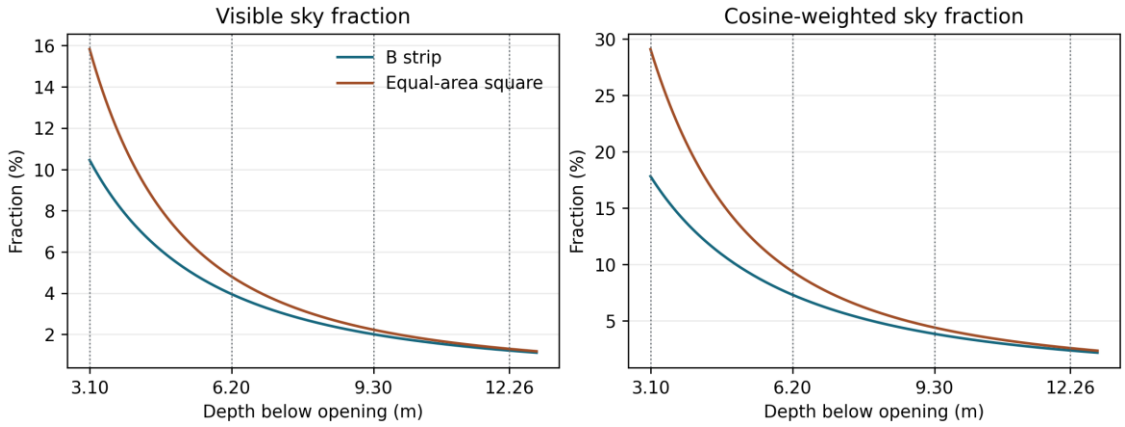


Figure 4. Visible and cosine-weighted sky fractions for B and its equal-area square benchmark as a function of depth. Dotted guides mark all four case-derived model depths. The calculation assumes a continuous rectangular prism and direct access to the sky at the aperture plane.

4.3 Sensitivity to point location and rounding

At equal relative offsets the long-axis displacement in B is 8.71 times the short-axis displacement. It gives the greater reduction in that protocol. At equal metric offsets the ordering reverses. For example, at 3.10 m the visible sky fraction of the strip is 10.425% after a 0.48 m long-axis shift and 10.190% after a 0.48 m short-axis shift, compared with 10.451% on axis. This reversal also occurs at each of the remaining tested depths. It establishes a dependence on the displacement protocol and does not establish a room-based directional effect.

Table 4. Off-axis visible sky fraction (%) under relative and metric protocols

Depth (m)	Strip relative long	Strip relative short	Square relative either	Strip 0.48 m long	Strip 0.48 m short	Square 0.48 m either
3.10	7.710	10.190	13.362	10.425	10.190	15.516
6.20	3.072	3.924	4.505	3.942	3.924	4.769
9.30	1.687	2.001	2.158	2.003	2.001	2.219
12.26	1.079	1.217	1.276	1.218	1.217	1.298

At 3.10 m, changing the strip length from 10.45 m to 10.40 m changes the axial result from 10.45% to 10.44%, while the independently resized equal-area square changes from 15.82% to 15.76%. Increasing the reference distance by 0.60 m instead, holding nominal dimensions fixed, gives 8.34% and 11.93% for the strip and square at 3.70 m. Applying the same increase at the deepest level gives 1.12% and 1.18% at 12.86 m.

4. Discussion

4.1. Implications for the Aqaba case

The drawing comparison identifies a reduction under the principal reading at all four surveyed levels. The strength of that result varies with the panel. The first and fourth floors retain a reduction across the tested interpretations and measurement bounds. The reduction

on the shared second/third-floor panel depends on how the combined uncertainties are treated. The architectural drawing, the annotated reading and the quantitative envelope are all needed to interpret this result.

In the independent aperture comparison, the proposed strip exposes more of the hemisphere on axis than the smaller proposed openings A and C. The equal-area square exposes more than the strip. The two comparisons demonstrate the importance of retaining geometric controls when attributing a difference to aspect ratio. Under a uniform-luminance sky the cosine-weighted figure describes the direct contribution to a horizontal receptor relative to an unobstructed one. The ordinary visible fraction measures an angular share of the hemisphere, without that weighting.

The axial advantage of the square under this model also follows directly from the equation. At fixed aperture area and depth, the numerator is constant. The denominator increases with the sum of the squared side lengths, which is minimized by equal sides. The square therefore maximizes the axial solid angle within the class of equal-area rectangles. The site-specific question is the magnitude of the difference at each reference depth.

The diminishing difference between the strip and square at depth is consistent with the far-field behavior of the solid-angle equation. At distances large relative to both aperture dimensions, the leading term depends on area and inverse squared distance. As the observation point moves nearer to the aperture, the distribution of the aperture around that point contributes more strongly. The shallower modeled depths therefore show a larger geometric difference between shapes. At greater depth, both apertures present only a small portion of the sky. This convergence applies to the modeled axial points.

An elongated shaft may serve a greater length of wall or a different set of apertures than a compact shaft. Figure 3 makes that possibility relevant because B spans a substantial portion of the rear of the footprint. The ranking is restricted to sky exposure under the stipulated geometry and observation points. The available drawings do not establish a feasible equal-area alternative or matched window positions and unobstructed sightlines for both design states. A room-based design comparison would have to incorporate the positions, elevations and glazing of attached windows, and may yield a different ranking across the set of rooms served.

4.2. Transferability and limits of inference

The study's workflow can be applied to projects with drawings that allow the existing and proposed void boundaries to be identified, the reference geometry to be dimensioned, and the relevant level datums to be established. The drawing audit quantifies changes in plan void area and shows how alternative readings of ambiguous linework affect the estimated reductions. A room-level daylight assessment would require a continuous three-dimensional reconstruction of the path from each observation point to the sky, together with the relevant optical inputs.

The reported sensitivity bounds apply to the tested endpoint variations, the three interpretations of the rear boundary, and the discrepancy between the plan and schedule dimensions for opening B. Their scope is limited to the documented geometry and the scenarios evaluated. The roof datum provides a consistent reference for the aperture model. Actual sky visibility may also depend on shaft offsets and constrictions, coverings, overhangs, and adjacent structures.

The International Journal of Engineering Sciences
https://international-journal-of-engineering-sciences.jo
Vol. 2, No. 2, 2026, pp. 234-250
ISSN 3104-8897

For the old configuration, the percentage estimates describe changes in plan void area relative to the proposed layout. The sky-access analysis covers the proposed aperture dimensions and the hypothetical equal-area benchmark. Its findings therefore concern geometric sky access within the model. Quantifying changes in illuminance between the two layouts, assessing daylight gains in individual rooms, and evaluating energy use, glare, ventilation, or regulatory compliance would require additional data and analyses.

The numerical findings are specific to this case. The same integrals can be applied to rectangular apertures in other projects using their own dimensions, reference depths, and observation positions under the stated model assumptions. The drawing audit and aperture tests together help identify which sections and shaft constrictions warrant closer reconstruction in a subsequent daylight assessment.

5. Conclusion

The calibrated audit of sheet A-3 yielded nominal void-area reductions of 40.5%, 27.8%, 27.8% and 45.3% for the first through fourth floors, respectively. The first- and fourth-floor reductions remained positive across the combined sensitivity tests. For the second and third floors, which share a plan panel, the sensitivity bounds no longer established a reduction when the conservative rear-boundary interpretation was combined with the ±4-pixel endpoint variation.

In the equal-area aperture experiment, the centred visible sky fraction for the strip was 10.45% at a depth of 3.10 m and 1.22% at 12.26 m. The corresponding values for the square were 15.82% and 1.30%. Off-axis results depended on whether the displacement was held constant in metres or scaled to the aperture dimension along the tested axis.

The drawing audit quantified changes in plan void area, while the aperture experiment evaluated direct sky access under idealized conditions. Quantifying the renovation’s effect on sky access within the building would require verified three-dimensional sky paths from the same observation points in both configurations.

6. Data access and disclosures

Data access. The complete dataset will be provided in a supplementary PDF accompanying the main article. The supplementary file will be publicly accessible and freely available for download.

7. References

1. Amoruso, F. M., Dietrich, U., & Schuetze, T. (2019). Integrated BIM-Parametric Workflow-Based Analysis of Daylight Improvement for Sustainable Renovation of an Exemplary Apartment in Seoul, Korea. Sustainability, 11(9), 2699. https://doi.org/10.3390/su11092699
2. Alghaemdi, M. A., & Hale, J. (2026). Between Seeing and Moving: A Sequential Isovist Analysis of Liminal Spaces at the Kiasma Museum of Contemporary Art. Architecture, 6(3), 166. https://doi.org/10.3390/architecture6030166
3. Ghoussayni, F., Ali, A., & Bayyati, A. (2026). The theory of Void in architecture. Cogent Arts & Humanities, 13(1). https://doi.org/10.1080/23311983.2026.2650972
4. Wang, L., Ibrahim, A., & Jiang, Y. (2025). Multi-Objective Optimization of Atrium Form Variables for Daylighting, Energy Consumption and Thermal Comfort of Teaching Buildings at the Early Design Stage in Cold Climates. Buildings, 15(24), 4434. https://doi.org/10.3390/buildings15244434
5. Guan, Z., Xu, X., Xue, Y., & Wang, C. (2023). Multi-Objective Optimization Design of Geometric Parameters of Atrium in nZEB Based on Energy Consumption, Carbon Emission and Cost. Sustainability, 15(1), 147. https://doi.org/10.3390/su15010147
6. Acosta García, I. J., Navarro Casas, J., & Sendra, J. J. (2014). Lighting design in courtyards: Predictive method of daylight factors under overcast sky conditions. https://idus.us.es/server/api/core/bitstreams/f6dfc4bd-1021-4b8b-8a87-e2fb6944e202/content
7. Amin Alah Ahadi, Mahmoud Reza Saghafi, Mansoureh Tahbaz, The study of effective factors in daylight performance of light-wells with dynamic daylight metrics in residential buildings, Solar Energy, Volume 155, 2017, Pages 679-697, ISSN 0038-092X, https://doi.org/10.1016/j.solener.2017.07.005
8. Antoine Bugeat, 2020. Improving the daylighting performance of residential light wells by reflecting and redirecting approaches, 2020, Solar Energy. DOI: https://doi.org/10.1016/J.SOLENER.2020.07.099
9. Nasab, S. M. R. A., & Teimourtash, S. (2023). Improving daylight performance of residential light wells in dry-cold climate: Optimization and sensitivity analysis. Solar Energy, 264, 112048. https://www.researchgate.net/profile/Seyed-Mohammad-Reza-Adel-Nasab/publication/374290629_Improving_daylight_performance_of_residential_light_wells_in_dry-cold_climate_Optimization_and_sensitivity_analysis/links/65172708321ec5513c1eacd7/Improving-daylight-performance-of-residential-light-wells-in-dry-cold-climate-Optimization-and-sensitivity-analysis.pdf

The International Journal of Engineering Sciences
https://international-journal-of-engineering-sciences.jo
Vol. 2, No. 2, 2026, pp. 234-250
ISSN 3104-8897

8. Appendix A Drawing calibration and boundary readings

Coordinates have a top-left origin and follow the order left, right, top, bottom. Rasterization used pdftoppm -f 4 -l 4 -scale-to 2600 -png. Figure 1b records the calibration ticks. The upper and lower tick centres round to y = 79 and y = 698 in all three panels, giving a 619-pixel span. The PDF vector dimension axes project to x ≈ 1577.55, 1037.12 and 502.45 pixels for the first, shared second/third and fourth-floor panels respectively. The corresponding integer raster readings are (1577, 79)–(1577, 698), (1037, 79)–(1037, 698) and (502, 79)–(502, 698). The nearby inner line at about y = 681 does not terminate the dimension. The area calculations use the integer raster coordinates. To reproduce Tables 1 and 2, divide 15 and 20 m by the respective bounding spans in the panel reference, multiply the individual opening spans by the corresponding scale, and sum their products. For lower bounds apply −8 pixels to each opening span and +8 pixels to each reference span. Reverse the signs for upper bounds. Proposed void area is 3.70 + 12.54 + 1.00 m², with a 12.48 m² value for B under the fourth-floor alternative reading.

Table A1. Calibration and old-opening geometry in raster pixels

Plan panel	Reference footprint	Old opening rectangles
First	(1532, 1997, 79, 698)	(1959, 1990, 168, 200), (1897, 1996, 308, 385), (1862, 1996, 545, 688)
Second and third	(992, 1456, 79, 698)	(1318, 1450, 84, 200), (1357, 1455, 308, 385)
Fourth	(457, 922, 79, 698)	(784, 915, 84, 200), (822, 921, 308, 385), (638, 738, 385, 459)

To obtain the two alternative readings on the shared second/third panel and the fourth-floor panel, replace the top coordinate of the first listed old rectangle with 79 or 122 and keep all other coordinates fixed. In the threshold test for stroke width, count consecutive pixels with greyscale intensity below 200 through the center of each sampled vertical line. The eight horizontal transects, expressed as (x, y) at the measured line, are (457, 250), (992, 235), (1532, 215), (915, 188), (1450, 188), (822, 330), (1357, 330) and (638, 429). This is a local raster check, with the wider perturbation specified in Section 3.1.

9. Appendix B Calculation recipe for aperture metrics

For an aperture with horizontal half-spans $a/2$ and $b/2$, and a point at offsets u, v from the aperture axis, use $x_1 = -a/2 - u$, $x_2 = a/2 - u$, $y_1 = -b/2 - v$, and $y_2 = b/2 - v$. Define $F(x, y) = \arctan\left[xy/\left(h\sqrt{h^2 + x^2 + y^2}\right)\right]$. Then

$$\Omega = F(x_2, y_2) - F(x_1, y_2) - F(x_2, y_1) + F(x_1, y_1).$$

Use $(u, v) = (0,0)$ for Table 3, $(0.4a, 0)$ or $(0, 0.4b)$ for the relative checks and $(0.48, 0)$ or $(0, 0.48)$ for the equal-distance checks in Table 4. Aperture dimensions in metres are $(2.00, 1.85)$, $(10.45, 1.20)$, $(1.00, 1.00)$ and $\left(\sqrt{12.54}, \sqrt{12.54}\right)$. For numerical integration

use nodes q_i and weights w_i from Gauss–Legendre quadrature on $[-1,1]$. Evaluate the integrand at $x_i = aq_i/2 - u$ and $y_j = bq_j/2 - v$ and multiply the weighted sum by $ab/4$. Use $h/\left(h^2 + x_i^2 + y_j^2\right)^{3/2}$ for the solid angle and $h^2/\left(h^2 + x_i^2 + y_j^2\right)^2$ for the projected integral. Divide by 2π and π, respectively, and multiply by 100 for the reported percentages.

Data access

The complete dataset will be provided in a supplementary PDF accompanying the main article. The supplementary file will be publicly accessible and freely available for download.

Ethical Considerations

Not applicable. This study did not require ethical approval because it does not include human or animal subjects and does not involve any personal or sensitive data.

List of Abbrevations:

Acknowledgment:

The author would like to express their sincere gratitude to **The International Journal of Engineering Sciences** - Noor Al-Ilm for Publishing and Distribution for their generous support in waiving all publication fees and facilitating the publication of this manuscript free of charge. Their commitment to promoting scientific research and supporting researchers is highly appreciated.

Author Contribution:

Author Contributions: All authors contributed equally to the main contributor to this paper. All authors read and approved the final paper

The International Journal of Engineering Sciences
https://international-journal-of-engineering-sciences.jo
Vol. 2, No. 2, 2026, pp. 234-250
ISSN 3104-8897

Declaration of generative AI and AI-assisted technologies in the writing process

The authors hereby declare that no generative artificial intelligence or AI-assisted technologies were used at any stage during the preparation of this manuscript, including language editing, proofreading, or content development. The authors take full responsibility for the originality and integrity of the work presented in this publication.

Funding:

This research received no external financial funding. The authors also acknowledge **The International Journal of Engineering Sciences**, Noor Al-Ilm for Publishing and Distribution, for providing a full waiver of the publication fees. The publication fee waiver was provided as editorial support and did not involve any financial contribution to the conduct, design, analysis, or reporting of the research.

Conflicts of Interest:

"The authors declare no conflict of interest."